

# Harnessing moiré ferroelectricity to modulate semiconductor monolayer light emission

Dong Seob Kim<sup>1,2</sup>, Chengxin Xiao<sup>3</sup>, Roy C. Dominguez<sup>4</sup>, Zhida Liu<sup>1,2</sup>, Hamza Abudayyeh<sup>1,2</sup>,  
Kyoungpyo Lee<sup>1,2</sup>, Rigo Mayorga-Luna<sup>4</sup>, Hyunsue Kim<sup>1,2</sup>, Kenji Watanabe<sup>5</sup>, Takashi Taniguchi<sup>6</sup>,  
Chih-Kang Shih<sup>1,2</sup>, Yoichi Miyahara<sup>4,7</sup>, Wang Yao<sup>3</sup> and Xiaoqin Li<sup>1,2\*</sup>

<sup>1</sup>*Department of Physics and Center for Complex Quantum Systems, The University of Texas at Austin, Austin, Texas, 78712, USA.*

<sup>2</sup>*Center for Dynamics and Control of Materials and Texas Materials Institute, The University of Texas at Austin, Austin, Texas, 78712, USA.*

<sup>3</sup>*New Cornerstone Science Laboratory, Department of Physics, The University of Hong Kong, Hong Kong, China.*

<sup>4</sup>*Department of Physics, Texas State University, San Marcos, Texas, 78666, USA.*

<sup>5</sup>*Research Center for Electronic and Optical Materials, National Institute for Materials Science, 1-1 Namiki, Tsukuba 305-0044, Japan.*

<sup>6</sup>*Research Center for Materials Nanoarchitectonics, National Institute for Materials Science, 1-1 Namiki, Tsukuba 305-0044, Japan.*

<sup>7</sup>*Materials Science, Engineering and Commercialization Program (MSEC), Texas State University, San Marcos, Texas, 78666, USA.*

Corresponding authors: [elaineli@physics.utexas.edu](mailto:elaineli@physics.utexas.edu)

May 21, 2024

**Ferroelectricity has been recently discovered in stacked or twisted van der Waals (vdW) moiré systems. The versatility of producing a large array of size-tunable domains and integration with diverse functional materials make them an enticing platform for developing multifunctional devices. Here, we show that ferroelectric polar domains formed in a twisted hexagonal boron nitride (t-hBN) substrate can modulate light emission from an adjacent semiconductor monolayer. The abrupt change in electrostatic potential across the domains produces an in-plane electric field (E-field) and leads to a remarkably large exciton Stark shift in the adjacent MoSe<sub>2</sub> monolayer, previously only observable in *p-n* junctions created by the advanced e-beam lithography tools. Both the spectrum and spatial pattern of the light emission from the monolayer are periodically modulated by the remote moiré potential imposed by the t-hBN substrate. We further observe a characteristic hysteresis behavior in the light emission as an electric gate erases and restores the domains. Our findings chart an exciting pathway for integrating nanometer-scale moiré ferroelectric domains with various optically active functional layers, paving the way for advanced nanophotonic applications.**

Moiré superlattices formed by stacking two van der Waals (vdW) layers present seemingly endless possibilities for engineering material properties with immense potential for electronic and photonic applications. While transition metal dichalcogenide (TMD) monolayers have already found many applications as essential functional layers in field effect transistors<sup>1-3</sup>, optical modulators<sup>4,5</sup>, detectors<sup>6,7</sup>, and light-emitting devices<sup>8,9</sup>, their properties become far more tunable when a moiré superlattice is constructed. The optical spectra of TMD moiré superlattices feature prominent exciton resonances whose resonant energies, lifetimes, and transport all depend on the twist angle<sup>10-12</sup>. However, these properties change simultaneously, imposing some undesirable constraints. For example, as the lateral confinement size reduces with an increasing twist angle,

the exciton lifetime increases, likely leading to a reduced quantum yield<sup>13,14</sup>.

Remote Coulomb engineering has been proposed as a possible solution to overcome this challenge. When a TMD monolayer is placed near a moiré superlattice formed between graphene/hBN or magic-angle graphene bilayers<sup>15–17</sup>, new exciton resonances, typically replicas of higher energy excited states (e.g. 2s exciton), have been observed. In these previous studies, higher energy exciton states in TMD monolayers are used as sensors when the correlated states formed in the adjacent moiré superlattice change its dielectric constant<sup>18</sup>. Because no such replica associated with the most prominent 1s excitons has been observed, remote electrostatic potential has been ruled out as a mechanism for modifying the optical spectra of TMD monolayers<sup>15</sup>. Twisted hBN substrate has been suggested as an alternative platform for expanding the strategy of moiré engineering to a broad range of functional layers due to its deep surface electrostatic potential and high band gap<sup>19</sup>. Hexagonal BN has become increasingly relevant as a photonic material for hosting quantum defect emitters<sup>20,21</sup>, detecting UV light<sup>22</sup>, or as a natural hyperbolic material in the mid-IR range<sup>23,24</sup>. Very recently, slid or twisted hBN bilayers with a parallel interface have been found to exhibit ferroelectricity<sup>25,26</sup>.

Here, we unveil an innovative strategy that seamlessly integrates the newly found ferroelectricity in twisted hBN with the light-emitting properties of a semiconductor monolayer. We find that the electric field (E-field) present at the domain walls (DWs) of t-hBN FE polar domains modulates both the spectrum and spatial pattern of light emission from an adjacent MoSe<sub>2</sub> monolayer. The in-plane E-field is sufficiently large to induce a Stark-shifted exciton ( $X_{\text{Stark}}$ ) spectrally separated from the original excitons ( $X_0$ ) residing within the domains. By correlating Kelvin Probe

Force Microscopy (KPFM) and optical microscopy experiments, we show spatial modulations of light emission following the moiré pattern of the t-hBN substrate. Upon erasing and restoring the FE domains, the light emission from the MoSe<sub>2</sub> monolayer exhibits hysteresis behavior, characteristic of ferroelectricity from the t-hBN substrate. Because the FE domain size is readily controlled by the twist angle, the light emission pattern can be modulated at a length scale far below the optical diffraction limit, charting a new pathway for shaping structured light<sup>27,28</sup>.

We first explain the formation of FE domains in a t-hBN bilayer conceptually as depicted in Fig. 1a. A natural hBN crystal consists of layers stacked in AA' sequence, in which hexagonal lattices overlap, and B (N) atoms are vertically aligned with corresponding N (B) atoms in adjacent layers. In another energetically favorable AB or BA (Bernal) stacking configuration, in which hexagonal lattices laterally slide, the B (N) atoms in the upper layer align with the N (B) atoms in the lower layer, and the N (B) atoms in the upper layer are positioned above the vacant center of the hexagon in the lower layer. The spatial inversion symmetry is broken, leading to opposite polarization directions between AB and BA stacking as indicated by the black arrows.

An array of FE domains with alternating polarization directions are formed in a t-hBN bilayer in which the domain size is readily controlled by the twist angle. These FE domains can be directly visualized via KPFM shown in Fig. 1b as an example. Details of the sample preparation and KPFM measurements can be found in Methods. The color contrast in a KPFM image represents the electrostatic potential near the top surface of the t-hBN, which is related to polarization via

$$V(\mathbf{R}, z) \approx \text{sgn}(z) \frac{P(\mathbf{R})}{2\epsilon_0} e^{-G|z|}, \quad (1)$$

where the net polarization is calculated from  $P(\mathbf{R}) = \int z' \Delta\rho(\mathbf{R}, z') dz'$ ,  $G = \frac{4\pi}{\sqrt{3}b}$ ,  $\mathbf{R}$  represents

the lateral position vector,  $b$  characterizes the supercell size, and  $z$  is the vertical distance to the buried interface<sup>19</sup>. The magnitude of  $P$  is  $2.01 \text{ pCm}^{-1}$  obtained from the first principles calculations. The surface potential extracted from KPFM measurements agrees remarkably well with the prediction of this theory<sup>29</sup>. When a semiconductor functional layer is placed on top of a t-hBN substrate, the E-field (green lines in Fig. 1c) generated by the surface potential of the t-hBN can periodically modulate the spectral and spatial pattern of the semiconductor layer as illustrated in Fig. 1d.

We examine the in-plane E-field developed at the DWs due to an electrostatic potential drop between adjacent domains (Fig. 2a). The in-plane E-field was calculated using a supercell size of 500 nm and a top thickness of t-hBN of 4.8 nm. The side view of E-field vectors at the DW is plotted in Fig. 2b. We hypothesize that the in-plane E-field at the DWs separates the electron and hole without dissociating the excitons in  $\text{MoSe}_2$  as illustrated in Fig. 2c. To verify this hypothesis, we conduct experiments by placing a  $\text{MoSe}_2$  monolayer on a t-hBN substrate with large domains identified via the KPFM image shown in Fig. 2d. In this particular structure, the separation between the  $\text{MoSe}_2$  monolayer and the twisted hBN interface, i.e. the top t-hBN thickness, is  $\sim 12 \text{ nm}$ .

Optical reflectivity measurements are taken from three locations across the DW as indicated by the red arrow in Fig. 2d. The derivatives of reflectance spectra are displayed in Fig. 2e. The three stacked spectra (bottom to top) are labeled by their respective locations shown in Fig. 2d. While spectra 1 and 3 taken within a domain feature one exciton resonance, an additional exciton resonance is observed in spectrum 2 taken from a region that overlaps with the DW. We fit these resonances using Lorentzian functions (solid lines in Fig. 2e). The exciton resonance measured

within the AB and BA domains (spectra 1 and 3) exhibits a small energy shift of  $\sim 1$  meV while the higher energy exciton in spectrum 2 lies in-between. Considering the spatial resolution of  $\sim 1.5 \mu\text{m}$ , this intermediate energy likely derives from averaging over excitons residing in the two adjacent and opposite FE domains. We attribute the lower energy exciton in spectrum 2 to exciton Stark shift due to the in-plane E-field at the DW as illustrated in Fig. 2c. The exciton Stark shift, or the separation between the two resonances is  $\sim 3$  meV in this case.

To establish Stark shift as the mechanism giving rise to the additional resonance at the DWs, we quantitatively evaluate the in-plane E-field,  $F_x = \Delta V_S/d_{\text{DW}}$  by measuring the potential drop ( $\Delta V_S$ ) across the DW ( $d_{\text{DW}}$ ) in multiple samples over regions with different domain sizes (Extended Data Fig. 2). To the first order, a quadratic relation between the E-field,  $F_x$ , and exciton Stark shift has been predicted  $E_{\text{shift}} = |-\frac{1}{2}\alpha F_x^2|$ , where  $\alpha$  is the exciton polarizability. We plot the exciton energy shift as a function of the in-plane E-field in Extended Data Fig. 1. Our experiment reports a slightly larger Stark shift or higher exciton polarizability than previous studies<sup>30,31</sup>. This difference may arise from either an underestimated E-field due to a finite tip-sample distance or our specific fitting procedure used to extract the E-field from the KPFM measurements.

Since the in-plane E-field and the  $X_{\text{Stark}}$  are only present at the DWs, one expects not only a spectral but also a spatial modulation of the light emission from the functional semiconductor layer placed on top of the t-hBN with an array of FE domains. We model the electrostatic potential and the corresponding exciton Stark shift induced by an in-plane E-field in the MoSe<sub>2</sub>/t-hBN heterostructure shown in Fig. 3a-b (details in Method). We then compare the KPFM image (Fig. 3c) and confocal photoluminescence image (Fig. 3d) taken from a MoSe<sub>2</sub> monolayer placed on the

t-hBN substrate. In Fig. 3d, we plot the integrated intensity ratio of  $X_{\text{Stark}}$  and  $X_0$  and observe a spatial correlation between the  $X_{\text{Stark}}$  intensity and the DWs (dashed red lines). Because our measurements are constrained by the optical diffraction limit, we can only image  $\sim 500$  nm or larger domains in our current experimental setup. In principle, light emission modulated by a vdW FE substrate can be used to generate structured light emission on a few nanometer length scales defined by the moiré supercells, far below the optical diffraction limit.

Finally, we demonstrate how an electric gate can be used to modulate light emission from MoSe<sub>2</sub> by repeatedly erasing and restoring the FE domains of t-hBN substrates. To accomplish this, we fabricate a dual-gate device structure as illustrated in Fig. 4a. The device is built on the same stacked layers measured in Fig. 1c in which the MoSe<sub>2</sub> monolayer is separated from the t-hBN interface by 12 nm. We measure a series of reflection spectra (Fig. 4b) as the vertically applied E-field,  $V_B/d_B$  is varied while keeping the MoSe<sub>2</sub> monolayer undoped (i.e. under the condition  $V_T/d_T + V_B/d_B = 0$ .) In the absence of a vertically applied E-field or a small E-field, exciton doublets are observed due to the exciton Stark shift at the DWs. When the vertically applied E-field is sufficiently large, (i.e., above  $V_B/d_B = \pm 0.2$  V/nm), the exciton resonance subject to the Stark shift disappears. We summarize the exciton Stark shift as a function of the vertically applied E-field in Fig. 4d (see Extended Data Fig. 3 for more details). At a large applied E-field exceeding the critical value, the domain polarization is flipped<sup>26,32,33</sup> such that electrostatic potential from the hBN substrate becomes constant as illustrated in Fig. 4c. Consequently, the in-plane E-field vanishes and the  $X_{\text{Stark}}$  resonance disappears.

Remarkably, we observe a hysteresis behavior of exciton Stark shift in Fig. 4d as the gate

voltage is swept forward (blue circles) and backward (red circles). This behavior is attributed to the ferroelectricity of the t-hBN substrate. We further demonstrated that this FE switching is reversible and robust over many switching cycles as shown in Fig. 4e. The bottom gate and top gate are both changed in the range of -6 to 6 V to keep the MoSe<sub>2</sub> layer charge neutral. The necessary switching voltage depends on the hBN thickness. The FE domain switching is measured via the exciton Stark shift. Over several cycles, the Stark shifted exciton energy drifts, which likely arise from the DW distortions (Extended Data Fig. 3) <sup>33,34</sup>. Optical spectroscopy data are typically averaged over several domains except in special cases where we intentionally choose to perform experiments along the DW of a large domain greater than several microns (e.g. Fig. 2b-c).

We discuss our findings in the context of previous studies. A large in-plane E-field is often present in *p-n* junctions, ubiquitous in semiconductor devices. Indeed,  $X_{\text{Stark}}$  in TMD monolayers have been observed in *p-n* junctions defined by lithographic patterns <sup>35,36</sup>. An exciton Stark shift of a few meV similar to our observation is observable only with a large gate voltage of 10 - 20 V. The intrinsic region in such gate-defined *p-n* junctions (40 - 60 nm) is wider than the DWs (< 10 nm) of t-hBN substrates. Thus, our study suggests a compelling lithography-free technique of creating a regular array of narrow semiconductor junctions by placing the functional layer on top of a t-hBN substrate. We note that similar multi-functional junctions have never been realized in heterostructures consisting of TMD thin layers placed on conventional FE substrates <sup>27,37,38</sup>. Conventional FE substrates usually have atomically sharp DWs <sup>39,40</sup> and the in-plane E-field generated by a conventional FE substrate is so strong ( $\sim 400$  mV/nm) that excitons are often dissociated <sup>38</sup>. In contrast, the in-plane E-field at the surface of t-hBN substrates studied is on the order of  $\sim 20$

mV/nm, which is significantly smaller than the binding energy ( $\sim 200$  meV) of excitons in TMD monolayers<sup>41</sup>. Combined with the few-nanometer DW width in t-hBN, it can effectively control and confine excitons and carriers in the semiconductor layer.

In conclusion, we demonstrate that a t-hBN substrate can modulate the light emission from an adjacent semiconductor layer both spectrally and spatially. The in-plane E-field introduced at the FE DWs is sufficiently large to induce a distinct Stark-shifted exciton resonance, similar to that found in semiconductor junctions typically created with advanced lithograph tools. The light emission can be further modulated by an electric gate that erases and restores the FE domains in the t-hBN. The hysteresis behavior observed in optical spectra demonstrates that the ferroelectric property of the t-hBN substrate is successfully combined with the light emission functionality of the semiconductor layer. Our findings open the exciting possibilities for designing new optoelectronic devices based on TMD/FE-hBN heterostructures. For example, FE tuning of exciton resonances may facilitate coupling to optical cavities, enabling polariton-based photonic devices.

## Methods

**Sample preparation:** We exfoliated hBN flakes using scotch tape onto 285 nm SiO<sub>2</sub>/Si substrates. After choosing a target hBN flake via microscope imaging, nitrogen gas is blown to facilitate the folding process. Samples typically fold along either zigzag or armchair directions. After stacking or folding, the samples are annealed up to 400°C for 4 hours under vacuum  $\sim 10^{-7}$  Torr to increase interface bonding by removing polymer residue. For the MoSe<sub>2</sub>/t-hBN device structure, pre-patterned Pt/Ti is prepared by photolithography. Then t-hBN substrate is transferred using a 15% PPC solution and dissolved into anisole. Then contact graphite, MoSe<sub>2</sub> monolayer, top hBN,

and top gate graphite are transferred in the same way.

**KPFM measurements:** Kelvin probe force microscopy (KPFM) measurements were performed using SmartSPM (Horiba) in two-pass frequency modulation KPFM (FM-KPFM) mode. All the data were taken by FM-KPFM mode. We used Pt-coated conductive cantilever probes with a nominal resonance frequency of 70 kHz and a spring constant of 2 N/m (OPUS 240AC-PP, Mikro-masch), and the Au-coated cantilevers with supersharp diamond-like carbon tips with a nominal resonance frequency of 150 kHz and a spring constant of 5 N/m (BudgetSensors SHR150). In the FM-KPFM mode of SmartSPM, the resonance frequency shift of the mechanically excited oscillations (amplitude 20 nm), which are caused by the electrostatic force gradient with respect to the tip-sample distance, is detected via the phase of the cantilever oscillations. The amplitude of the modulation of the phase, which is caused by applying an ac voltage (3 V, 1 kHz), is proportional to the difference between the applied dc bias voltage between the contact potential difference (CPD) and is fed into a feedback controller to nullify the electrostatic force.

**Optical spectroscopy measurements:** For optical reflectivity measurements at 14 K, a compact stabilized broadband light source was focused to a spot size of  $\sim 2 \mu\text{m}$  in diameter using a 100 X microscope objective. For photoluminescence measurements, a He-Ne laser was used, and the excitation power was kept below  $5 \mu\text{W}$  to avoid local heating. The spatial mapping of photoluminescence was conducted in confocal geometry.

**Computational methods:** Extending the formula in <sup>19</sup> to a non-rigid twist region by considering all the reciprocal vectors, we can calculate the static electric potential at any position,

$$V(\mathbf{R}, z) \approx \sum_{\mathbf{G}} \frac{\tilde{P}(\mathbf{G})}{2\epsilon_0} e^{i\mathbf{G}\cdot\mathbf{R}} e^{-|\mathbf{G}||z|} \quad (2)$$

where  $\tilde{P}(\mathbf{G})$  is the Fourier components of the electric dipole  $P(\mathbf{R}) = \int \Delta\rho(\mathbf{R}, z)zdz$ , with  $\Delta\rho$  denoting the differential charge density, and  $\mathbf{G}$  is the moiré reciprocal vectors. The strong lattice reconstruction in the marginally twisted hBN results in a narrow domain wall (DW) between AB and BA stacking. Former ab initio study <sup>42</sup> shows the DW width of strained bilayer hBN is around 8 ~ 10 nm. Thus, we calculated the electric potential and the electric field in Fig. 1, using Eqn. (2) with triangular modified  $P(\mathbf{R})$  and 8 nm DW width.

## References

1. Radisavljevic, B., Radenovic, A., Brivio, J., Giacometti, V. & Kis, A. Single-layer MoS2 transistors. Nature Nanotechnology **6**, 147–150 (2011).
2. Wang, H. et al. Integrated Circuits Based on Bilayer MoS2 Transistors. Nano Letters **12**, 4674–4680 (2012).
3. Sarkar, D. et al. A subthermionic tunnel field-effect transistor with an atomically thin channel. Nature **526**, 91–95 (2015).
4. Seyler, K. L. et al. Electrical control of second-harmonic generation in a WSe2 monolayer transistor. Nature Nanotechnology **10**, 407–411 (2015).
5. Sun, Z., Martinez, A. & Wang, F. Optical modulators with 2D layered materials. Nature Photonics **10**, 227–238 (2016).

6. Lopez-Sanchez, O., Lembke, D., Kayci, M., Radenovic, A. & Kis, A. Ultrasensitive photodetectors based on monolayer MoS<sub>2</sub>. Nature Nanotechnology **8**, 497–501 (2013).
7. Baugher, B. W. H., Churchill, H. O. H., Yang, Y. & Jarillo-Herrero, P. Optoelectronic devices based on electrically tunable p–n diodes in a monolayer dichalcogenide. Nature Nanotechnology **9**, 262–267 (2014).
8. Ross, J. S. et al. Electrically tunable excitonic light-emitting diodes based on monolayer WSe<sub>2</sub> p–n junctions. Nature Nanotechnology **9**, 268–272 (2014).
9. Withers, F. et al. Light-emitting diodes by band-structure engineering in van der Waals heterostructures. Nature Materials **14**, 301–306 (2015).
10. Wilson, N. P., Yao, W., Shan, J. & Xu, X. Excitons and emergent quantum phenomena in stacked 2D semiconductors. Nature **599**, 383–392 (2021).
11. Huang, D., Choi, J., Shih, C.-K. & Li, X. Excitons in semiconductor moiré superlattices. Nature Nanotechnology **17**, 227–238 (2022).
12. Mak, K. F. & Shan, J. Semiconductor moiré materials. Nature Nanotechnology **17**, 686–695 (2022).
13. Choi, J. et al. Moiré potential impedes interlayer exciton diffusion in van der Waals heterostructures. Science Advances **6**, eaba8866 (2020).
14. Choi, J. et al. Twist Angle-Dependent Interlayer Exciton Lifetimes in van der Waals Heterostructures. Physical Review Letters **126**, 047401 (2021).

15. Xu, Y. et al. Creation of moiré bands in a monolayer semiconductor by spatially periodic dielectric screening. Nature Materials **20**, 645–649 (2021).
16. Hu, Q. et al. Observation of Rydberg moiré excitons. Science **380**, 1367–1372 (2023).
17. He, M. et al. Dynamically tunable moiré exciton Rydberg states in a monolayer semiconductor on twisted bilayer graphene. Nature Materials 1–6 (2024).
18. Gu, J. et al. Remote imprinting of moiré lattices. Nature Materials 1–5 (2024).
19. Zhao, P., Xiao, C. & Yao, W. Universal superlattice potential for 2D materials from twisted interface inside h-BN substrate. npj 2D Materials and Applications **5**, 1–7 (2021).
20. Tran, T. T., Bray, K., Ford, M. J., Toth, M. & Aharonovich, I. Quantum emission from hexagonal boron nitride monolayers. Nature Nanotechnology **11**, 37–41 (2016).
21. Grosso, G. et al. Tunable and high-purity room temperature single-photon emission from atomic defects in hexagonal boron nitride. Nature Communications **8**, 705 (2017).
22. Maity, A., Grenadier, S. J., Li, J., Lin, J. Y. & Jiang, H. X. Hexagonal boron nitride neutron detectors with high detection efficiencies. Journal of Applied Physics **123**, 044501 (2018).
23. Dai, S. et al. Tunable Phonon Polaritons in Atomically Thin van der Waals Crystals of Boron Nitride. Science **343**, 1125–1129 (2014).
24. Caldwell, J. D. et al. Sub-diffractive volume-confined polaritons in the natural hyperbolic material hexagonal boron nitride. Nature Communications **5**, 5221 (2014).

25. Yasuda, K., Wang, X., Watanabe, K., Taniguchi, T. & Jarillo-Herrero, P. Stacking-engineered ferroelectricity in bilayer boron nitride. Science **372**, 1458–1462 (2021).
26. Vizner Stern, M. et al. Interfacial ferroelectricity by van der Waals sliding. Science **372**, 1462–1466 (2021).
27. Wu, G. et al. Programmable transition metal dichalcogenide homojunctions controlled by nonvolatile ferroelectric domains. Nature Electronics **3**, 43–50 (2020).
28. Forbes, A., de Oliveira, M. & Dennis, M. R. Structured light. Nature Photonics **15**, 253–262 (2021).
29. Kim, D. S. et al. Electrostatic moiré potential from twisted hexagonal boron nitride layers. Nature Materials **23**, 65–70 (2024).
30. Pedersen, T. G. Exciton Stark shift and electroabsorption in monolayer transition-metal dichalcogenides. Physical Review B **94**, 125424 (2016).
31. Xiao, K. et al. Exciton-exciton Interaction in Monolayer MoSe<sub>2</sub> from Mutual Screening of Coulomb Binding (2023). URL <http://arxiv.org/abs/2308.14362>.
32. Wang, X. et al. Interfacial ferroelectricity in rhombohedral-stacked bilayer transition metal dichalcogenides. Nature Nanotechnology **17**, 367–371 (2022).
33. Ko, K. et al. Operando electron microscopy investigation of polar domain dynamics in twisted van der Waals homobilayers. Nature Materials **22**, 992–998 (2023).

34. Molino, L. et al. Ferroelectric Switching at Symmetry-Broken Interfaces by Local Control of Dislocations Networks. Advanced Materials **35**, 2207816 (2023).
35. Massicotte, M. et al. Dissociation of two-dimensional excitons in monolayer WSe<sub>2</sub>. Nature Communications **9**, 1633 (2018).
36. Thureja, D. et al. Electrically tunable quantum confinement of neutral excitons. Nature **606**, 298–304 (2022).
37. Wen, B. et al. Ferroelectric-Driven Exciton and Trion Modulation in Monolayer Molybdenum and Tungsten Diselenides. ACS Nano **13**, 5335–5343 (2019).
38. Soubelet, P. et al. Charged Exciton Kinetics in Monolayer MoSe<sub>2</sub> near Ferroelectric Domain Walls in Periodically Poled LiNbO<sub>3</sub>. Nano Letters **21**, 959–966 (2021).
39. Gonnissen, J. et al. Direct Observation of Ferroelectric Domain Walls in LiNbO<sub>3</sub>: Wall-Meanders, Kinks, and Local Electric Charges. Advanced Functional Materials **26**, 7599–7604 (2016).
40. Xiao, Z., Poddar, S., Ducharme, S. & Hong, X. Domain wall roughness and creep in nanoscale crystalline ferroelectric polymers. Applied Physics Letters **103**, 112903 (2013).
41. Goryca, M. et al. Revealing exciton masses and dielectric properties of monolayer semiconductors with high magnetic fields. Nature Communications **10**, 4172 (2019).

42. Lebedev, A. V., Lebedeva, I. V., Knizhnik, A. A. & Popov, A. M. Interlayer interaction and related properties of bilayer hexagonal boron nitride: ab initio study. *RSC Advances* **6**, 6423–6435 (2016).

### **Data availability**

The data that support the plots within this paper and other findings of this study are available from the corresponding authors upon reasonable request. Source data are provided with this paper.

### **Acknowledgements**

The experiments are primarily supported by NSF MRSEC DMR-2308817 (D. S. K.), Army Research Office W911NF-23-1-0364 (K.L.), and NSF ECCS-2130552 (Z. L.). X.L. gratefully acknowledges support from the Welch Foundation Chair F-0014. C.X. and W.Y. acknowledge support by RGC of HKSAR (AoE/P-701/20, HKU SRFS2122-7S05), and the New Cornerstone Science Foundation. The work by R. C. D. and R. M-L. is supported by the NSF Partnership for Research and Education in Materials (PREM) (NSF award DMR-2122041). Y. M. acknowledges the support by the NSF CAREER (DMR-2044920) and NSF MRI (DMR-2117438) grants. The collaboration between X. L. and C. S. are enabled by the National Science Foundation through the Center for Dynamics and Control of Materials: an NSF MRSEC under Cooperative Agreement No. DMR-1720595 and DMR-2308817, which also supported the user facility where part of the experiments were performed. C.K.S. acknowledges support from the NSF grant nos. DMR-2219610, the Welch Foundation F-2164, and the US Air Force grant no. FA2386-21-1-4061 K. W. and T. T. acknowledge support from the JSPS KAKENHI (Grant Numbers 20H00354, 21H05233

and 23H02052) and World Premier International Research Center Initiative (WPI), MEXT, Japan.

### **Author contributions**

D. S. K. and X. L. conceived the project. D. S. K. fabricated samples with assistance from K. L.. D. S. K. carried out optical measurements with H. A. and Z. L.'s help, and R. C. D. and R. M-L. performed AFM and KPFM measurements. Electrical gating measurements were done by D. S. K. with contributions from H. K. and Z. L.. K. W. and T. T. synthesized hBN single crystals. C. X., and W. Y. proposed the theoretical model and performed the calculation. D. S. K. analyzed the data with contributions from C. X.. The first draft of the manuscript was written by D. S. K., C. K. S., Y. M., W. Y., and X. L.. All authors contributed to discussions.

### **Competing interests**

The authors declare no competing interests.

## Figures

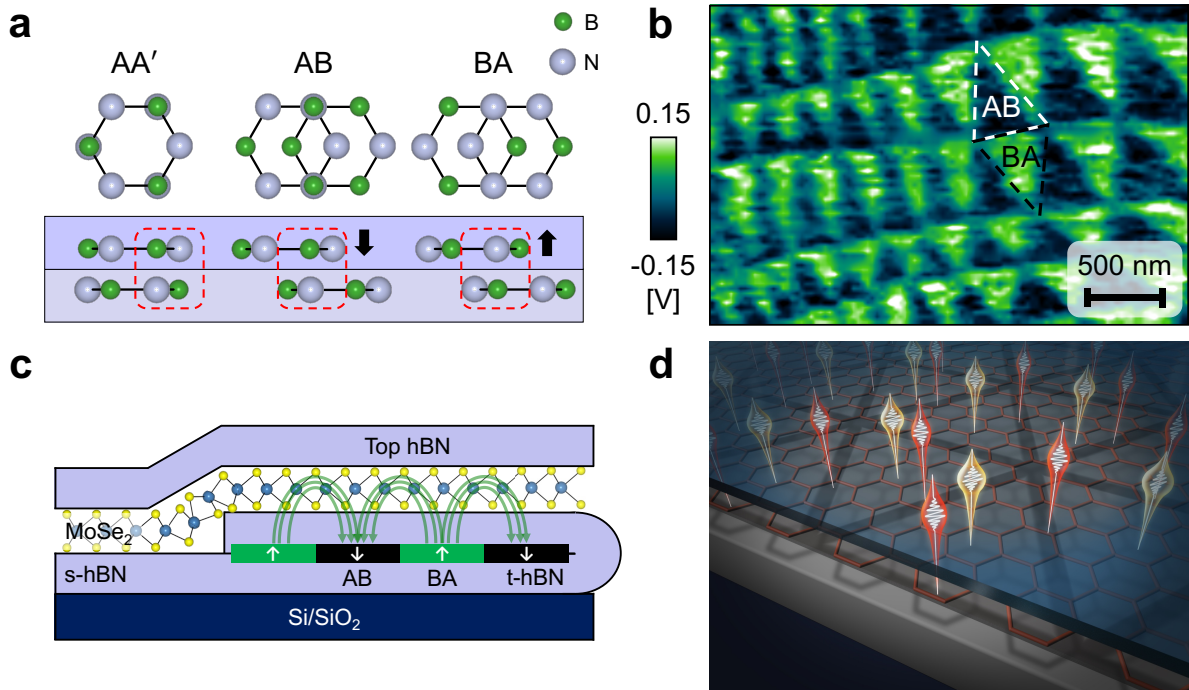


**Figure 1: Moiré ferroelectric domains in t-hBN modulate light emission from an adjacent semiconductor layer.** **a**, Top and side views of the hBN parallel interface at high-symmetry points. Inversion symmetry breaking leads to spontaneous polarization as indicated by down (up) black arrows corresponding to AB (BA) stacking. **b**, KPFM image of the electrostatic moiré potential on the top surface of a t-hBN substrate. AB (BA) domains are marked by white (black) dashed triangles. **c**, Sketch of a t-hBN/MoSe<sub>2</sub> monolayer/hBN vdW multilayer with alternating domains at the twisted hBN interface. Green lines and arrows illustrate the E-field generated by the FE domains with the largest in-plane E-field at the DWs. **d**, Illustration of spectral and spatial modulation of light emission from a semiconductor functional layer on top of a t-hBN substrate

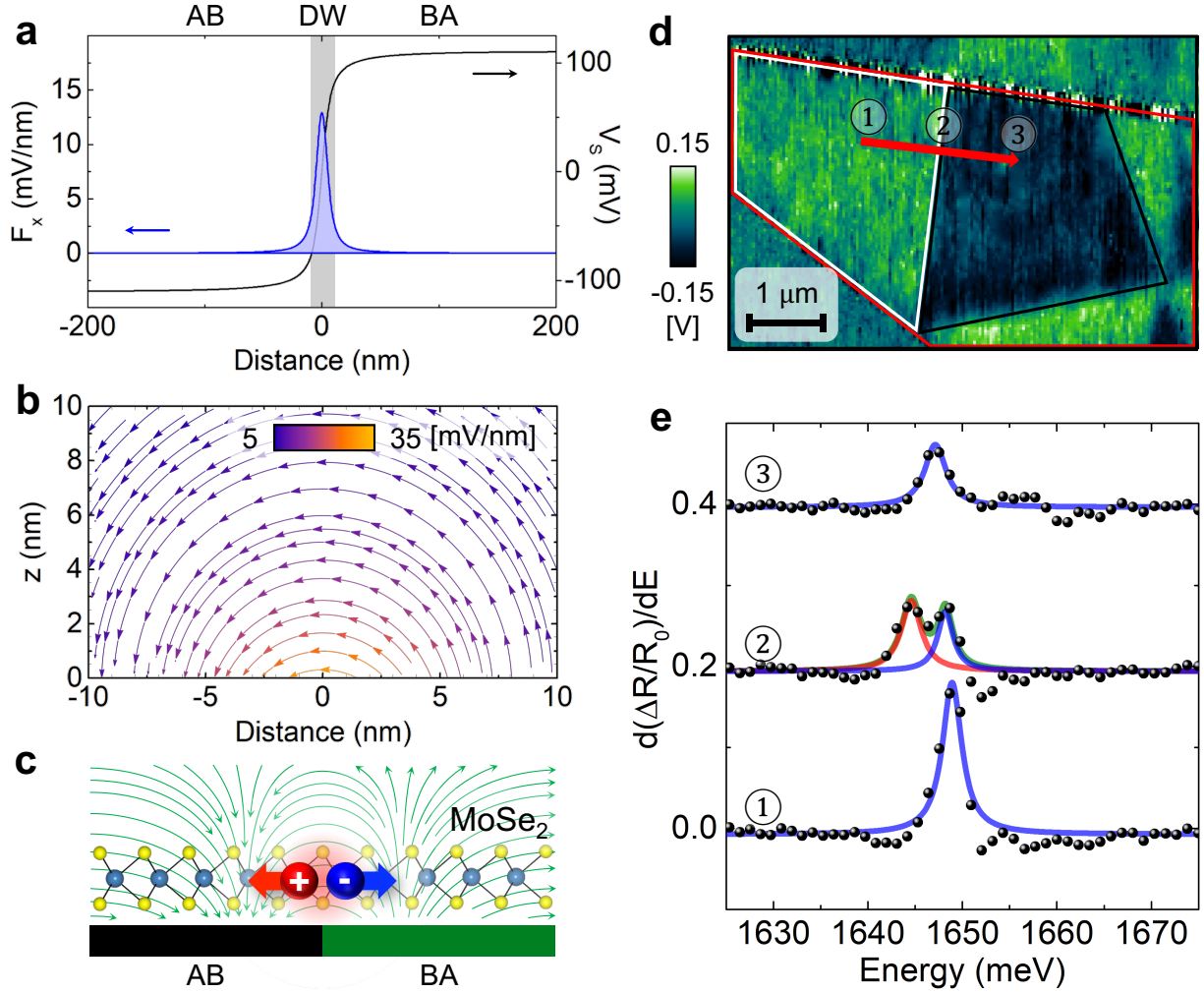


**Figure 2: Spectral modulation of light emission from MoSe<sub>2</sub> due to in-plane E-field at the DWs of a t-hBN substrate.** **a**, Calculated electrostatic potential (black) and in-plane E-field (blue) along a direction perpendicular to a DW. **b**, Side view of E-field lines near the DW. The color represents the field strength. **c**, The in-plane E-field at the DWs separates the electron and hole of an exciton and leads to a Stark-shifted exciton resonance. **d**, KPFM image of a t-hBN substrate forming large domains. Optical spectra are taken from a MoSe<sub>2</sub> monolayer at three locations along the red arrow. **e**, Derivative of reflectance contrast spectra from the MoSe<sub>2</sub> monolayer taken at three locations across two opposite and adjacent domains. The numbers correspond to the spots labeled in panel d. One exciton resonance is observed within the AB and BA domains while two resonances are observed at the DW.

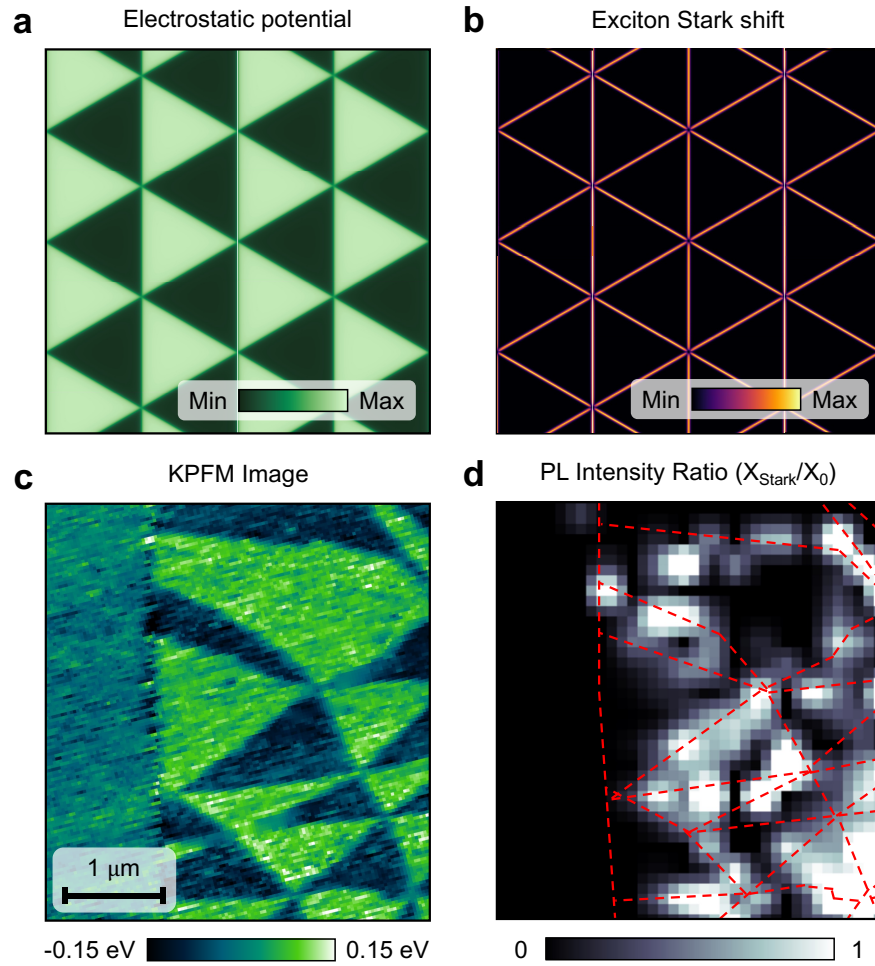


**Figure 3: Spatial modulation of light emission from MoSe<sub>2</sub> by a t-hBN substrate.** **a**, Simulated periodic moiré potential on top of a t-hBN substrate. **b**, Simulated exciton Stark shift from a MoSe<sub>2</sub> monolayer placed on a t-hBN substrate. **c**, KPFM image of the t-hBN substrate where PL spectra from an adjacent MoSe<sub>2</sub> monolayer are collected. **d**, Spatial map of integrated PL intensity ratio of two exciton resonances  $X_{\text{Stark}}/X_0$ . The DWs are marked by red dashed lines.

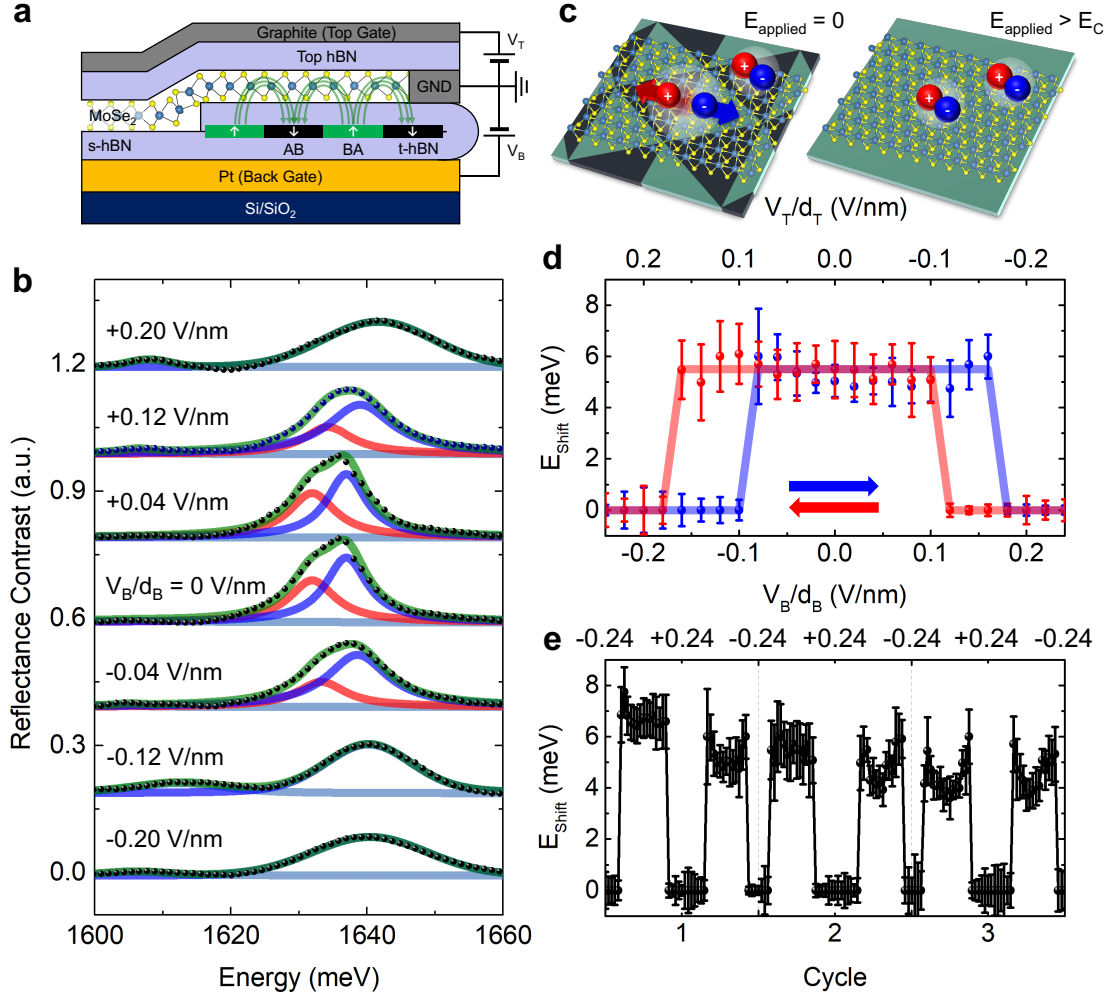
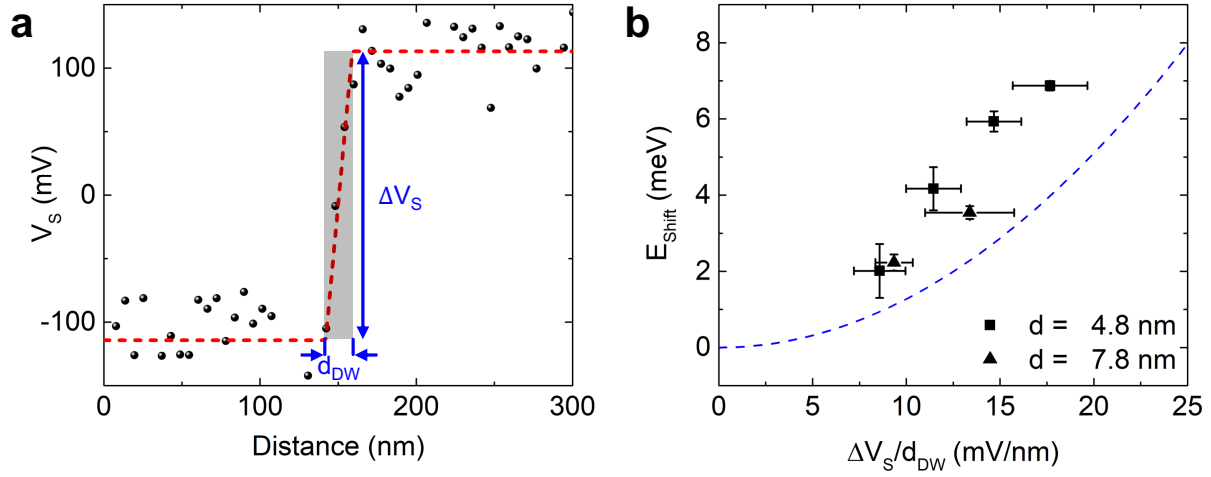
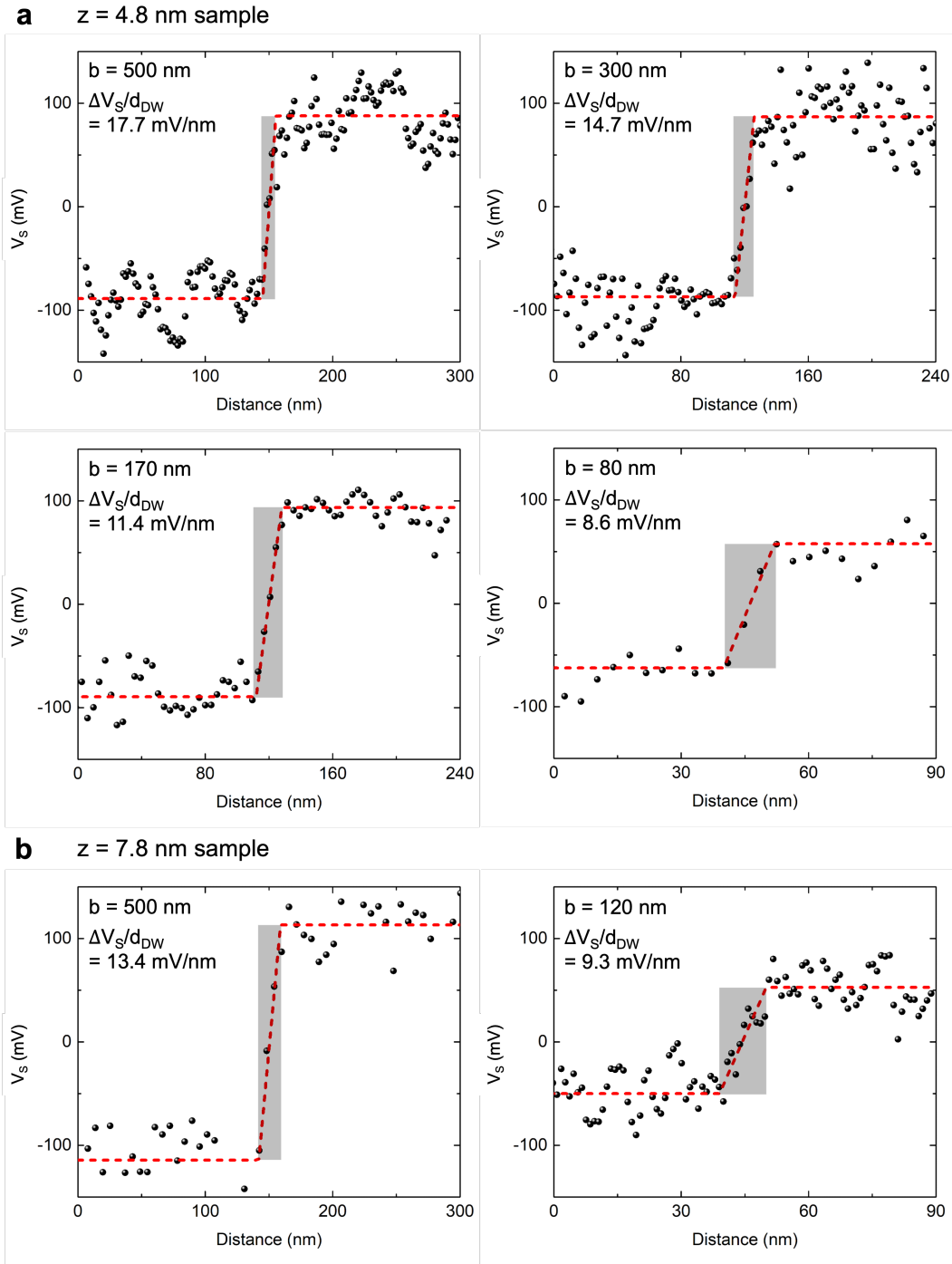


**Figure 4: Hysteresis of light emission demonstrating the combined functionality of the FE t-hBN substrate with the MoSe<sub>2</sub> monolayer.** **a**, Dual gate device structure. A MoSe<sub>2</sub> monolayer is placed on a t-hBN substrate and encapsulated by a top hBN layer. A vertical E-field is applied by adjusting the back-gate voltage  $V_B$  and top gate simultaneously while keeping the monolayer undoped. **b**, Reflectance spectra from the MoSe<sub>2</sub> monolayer placed on t-hBN substrate at different applied vertical E-fields. The exciton Stark shift from the FE domains is observed at  $V_B/d_B = 0$  Vnm<sup>-1</sup>. Above  $V_B/d_B = \pm 0.2$  Vnm<sup>-1</sup> (top), the  $X_{\text{Stark}}$  peak disappears. Circles are measured data and solid lines are Lorentzian fits. **c**, Illustration of field-driven switching of the FE domains of the t-hBN substrate as manifested via exciton resonances in the adjacent MoSe<sub>2</sub> monolayer. **d**, Exciton Stark-shift as a function of the applied E-field. The shift is constant until the resonance abruptly disappears above  $\pm 0.2$  Vnm<sup>-1</sup>. Blue (red) circles are measured exciton Stark-shift as the vertically applied E-field sweeps forward (backward). Hysteresis behavior is characteristic of ferroelectricity from the t-hBN substrate. The solid lines are a guide for the eye. Error bars represent the root mean square errors from the Lorentzian fitting to optical spectra. **e**, Multi-cycle switching of the FE domains manifested by exciton Stark shift. The switching field is  $\pm 0.24$  V/nm.

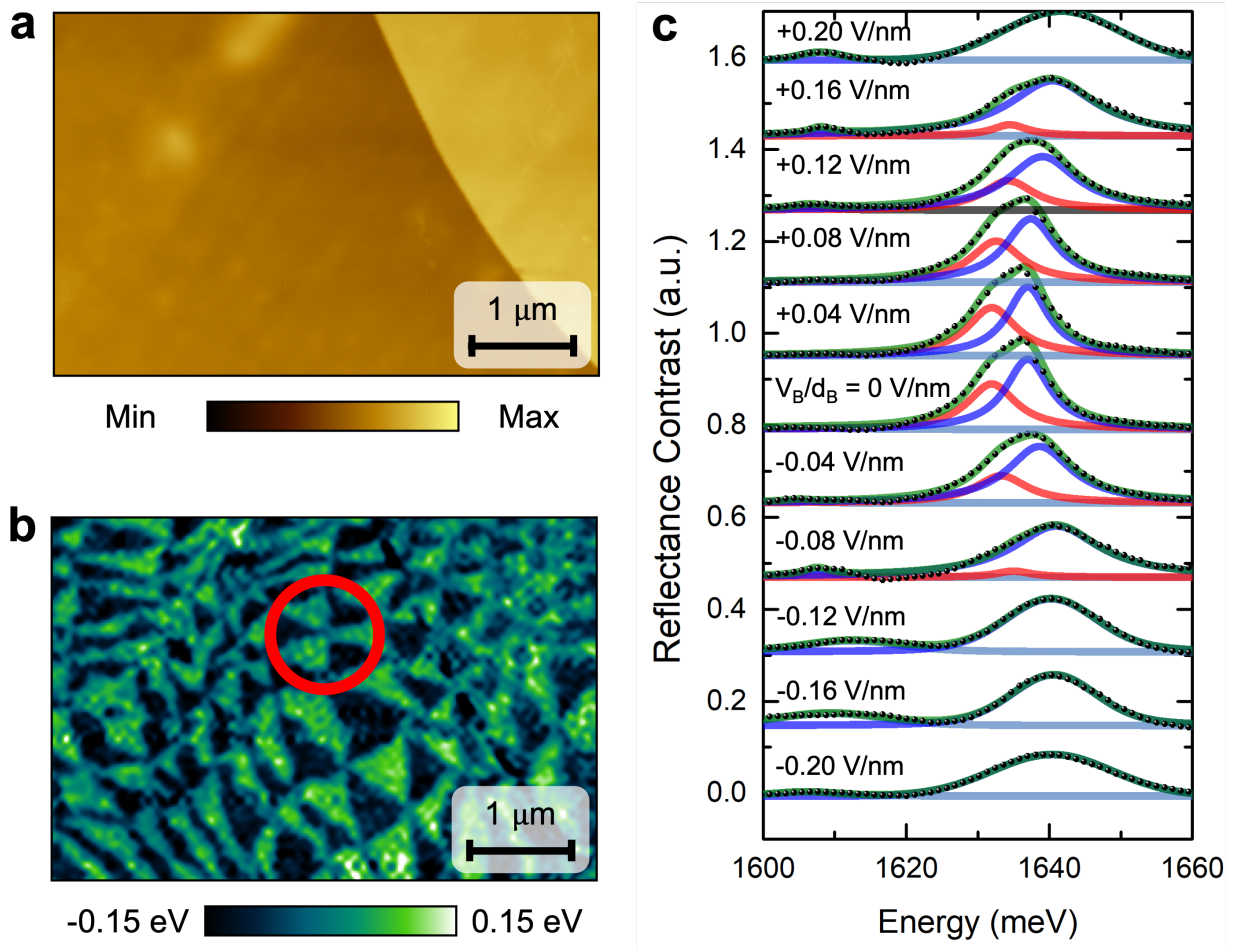
## Extended Data



**Extended Data Fig. 1: Dependence of Stark shift on in-plane E-field at the FE DWs at t-hBN substrate.** **a**, Electrostatic potential drops ( $\Delta V_s$  indicated by the vertical blue arrow) across the DW ( $d_{DW}$ ) of the t-hBN substrate, producing an in-plane E-field and causing exciton Stark shift. The grey strip indicates a finite DW thickness ( $d_{DW}$ ). The dashed red line is a guide for the eye. **b**, Summary of the exciton Stark shift as a function of the in-plane E-field, extracted from the KPFM measurements via  $\Delta V_s/d_{DW}$ . KPFM data are taken from two bare t-hBN substrates with different hBN thicknesses,  $d$ . The dashed blue line is the calculated exciton Stark shift. The error bars in the horizontal direction derive from both the  $\Delta V_s$  and  $d_{DW}$ . The error bars in the vertical direction are fitting errors in extracting the exciton energy splitting for spectra taken across DWs.



**Extended Data Fig. 2: Evaluation of the in-plane E-field for additional data points in Extended Data Fig. 1b.** **a, b,** KPFM line cuts showing electric potential drops across the DW of the t-hBN substrate with a thickness of **(a)** 4.8 nm and **(b)** 7.8 nm.



**Extended Data Fig. 3: Additional reflectance spectra from the MoSe<sub>2</sub>/t-hBN heterostructure used in Fig. 3d. a**, Topography of a t-hBN substrate. **b**, Corresponding KPFM image. The red circle indicates the location where the reflectance spectra were taken. **c**, Reflectance spectra from the MoSe<sub>2</sub> monolayer as the applied vertical E-field is varied.